This is the accepted manuscript made available via CHORUS. The article has been published as:

Rotational stability of twisted bilayer graphene

S. Bagchi, H. T. Johnson, and H. B. Chew

Phys. Rev. B **101**, 054109 — Published 25 February 2020

DOI: 10.1103/PhysRevB.101.054109

Rotational Stability of Twisted Bilayer Graphene

S. Bagchi[1], H. T. Johnson[2], H.B. Chew[1,*]

1. Department of Aerospace Engineering, University of Illinois at Urbana-Champaign, Urbana IL 61801, USA

2. Department of Mechanical Science and Engineering, Department of Materials Science and Engineering, and Materials Research Lab, University of Illinois at Urbana-Champaign, Urbana IL 61801, USA

*Author to whom all correspondence should be addressed. Email: hbchew@illinois.edu

Abstract

Moiré superlattices form in twisted graphene bilayers due to periodic regions of commensurability, but truncation of the moiré patterns affects the rotational stability of finite-sized sheets. Here, we report the stepwise untwisting of nanometer-sized bilayer graphene flakes at elevated temperatures, each step corresponding to a potential energy barrier formed by changes to the commensurability between the moiré superlattice and flake size with twist angle. The number of locally-stable energy states and their barrier energies scale with the flake size, allowing twisted graphene flakes of several tens of nanometers to remain thermally stable even at chemical vapor deposition temperatures.

Keywords: *Twisted bilayer graphene, structural transition, rotational stability, edge effects, moiré pattern*

1. Introduction

The successful isolation of graphene by exfoliating graphite has led to the realization of many other 2D atomic sheet structures [1]. With appropriate methods, atomic sheets of the same or different types can be stacked together in precise sequences to form a variety of layered 2D materials [2]. Changing the orientation of one layer with respect to another provides an additional degree of freedom to manipulate the weak van der Waals forces binding the layers together, resulting in layered structures with tailorable properties [3]. Bilayer graphene represents the simplest 2D multilayered structure. In its unrotated form, bilayer graphene exists in a Bernal (AB)-stacked configuration, which is the repeated stacking sequence of crystalline hexagonal graphite. Such perfectly-stacked bilayer structures have been synthesized by mechanical exfoliation or chemical vapor deposition (CVD) processes [1,2,4]. Selected area electron diffraction and dark-field transition electron microscopy (TEM) studies confirm the presence of twisted regions in CVD grown bilayer graphene patches [5]. Recent studies have now established synthesis protocols to enable twisting of bilayer graphene to change the stacking order, thus yielding a new class of low-dimensional carbon materials [3,6,7].

Twisted bilayer graphene can display a wide spectrum of unusual properties, including superlubricity [8–10], superconductivity [11], and ferromagnetism [7,12], due to changes in interlayer coupling with twist angle. An important parameter determining interlayer coupling is the period of the commensurate unit cell, termed the moiré superlattice, which varies significantly with small changes in the twist angle. The rotational stability of these twisted structures underpins material performance [13]. Friction force microscopy (FFM) studies show that cleaved, twisted graphitic flakes on graphite surfaces can undergo smooth sliding (superlubricity), followed by sudden termination of sliding associated with rotation of the graphene flake back to its commensurate AB-stacking [8,9,14–16]. Conversely, transition from a commensurate (AB-stacked) to an incommensurate (twisted) registry of the graphene flakes followed by sliding have also been observed [10]. Molecular statics calculations have reported the existence of potential energy barriers for untwisting of the graphene flakes [12,16], but the origin of these energy barriers in relation to the flake size, as well as the thermal stability (e.g. under CVD growth conditions) are not well understood. Here, we demonstrate that finite edge effects arising from truncation of the periodic moiré patterns generate a multiplicity of potential energy barriers for untwisting of the graphene flake at discrete twist angles. The number and magnitude of these energy barriers scales with the flake size, and result in size-dependent thermal stability of the rotational states.

2. Computational Methods

We study the rotational stability of twisted bilayer graphene with large-scale molecular dynamics (MD) simulations using LAMMPS [17]. We create model structures of finite-size, twisted bilayer graphene by rotating AB-stacked graphene flake on a freely-suspended infinite graphene sheet with an initial twist misorientation angle of $\theta = 7.34°$ about the out-of-plane axis (Fig. 1a). The superposition of the two twisted graphene lattices at this twist angle creates moiré patterns of periodicity $L_p = 1.9$ nm (Fig. 1b). Each moiré unit cell consists of atoms with several distinct stackings, termed as AB, AA, BA, and SP (Fig. 1c). We crop the graphene flake (top sheet) to conform to the dimensions of the moiré unit cell, i.e. the graphene flake has exactly 1 moiré period at $\theta = 7.34°$ and is termed $L1 \times L1$. We periodically replicate this unit cell 2, 4, 6, and 32 times in the in-plane directions to obtain $L2 \times L2$, $L4 \times L4$, $L6 \times L6$, and $L32 \times L32$ graphene flakes with corresponding rhombic edge dimensions of 3.8 nm, 7.6 nm, 11.4 nm, and

61.4 nm, respectively. We select the shape of the flake to be integral multiples of the moiré unit cell to allow a systematic study of the flake size effects relative to the period of the moiré unit cell, without introducing shape effects. The bottom periodic graphene sheet is modeled to be several times larger than the largest $L32 \times L32$ graphene flake, while a 20 nm thick vacuum layer in the out-of-plane direction is included in our fully-periodic simulation box.

In our bilayer graphene model, the in-plane C-C bonded interactions are described by the Reactive Empirical Bond Order (REBO) potential [18], while the non-bonded interlayer interactions are represented by a registry-dependent Kolmogorov-Crespi potential [19] which correctly captures the magnitude and anisotropy of the interlayer potential energy surface consistent with first principles calculations [20]. We have separately performed stacking fault energy (SFE) calculations of AB-stacked bilayer graphene using these potentials. The obtained SFEs are within 2% difference of those obtained from our Density Functional Theory (DFT) calculations using local density approximation as well as DFT calculations that account for van der Waals interactions [20].

3. Results

The above twisted graphene flakes are thermally equilibrated at temperatures ranging from 300 K to 3000 K with a Berendsen thermostat for 1 ns, followed by a Nose-Hoover thermostat for 3 ns (fixed time step of 1 fs). Figure 2a-d shows the change in twist angle for an $L4 \times L4$ graphene flake over the 4 ns equilibration period at various temperatures. At 300 K, the graphene flake rotates from its initial twist angle of $\theta = 7.34°$ to a larger twist angle of $\theta = {\sim}8°$ (Fig. 2a). At 600 K, however, the graphene flake rotates in a reverse direction (untwists) to $\theta = {\sim}6.4°$ (Fig. 2b). Higher temperature of 640 K drives the step changes in twist angle, first from $\theta = 7.34°$ to $\sim 6.4°$ at ~0.25 ns, and next to $\theta = \sim 4.5°$ at 0.5 ns, and finally to $\theta = \sim 2.6°$ at 2.25 ns (Fig. 2c). At slightly higher temperature of 650 K, the graphene flake instantaneously untwists to recover its AB-stacked configuration at $\theta = 0°$ (Fig. 2d). These distinct transitional rotations of the graphene flake are accompanied by changes to the moiré pattern and periodicity (Fig. 2g). Interestingly, these transitional rotations of the graphene flake are strongly size-dependent. For a smaller $L1 \times L1$ graphene flake, an instantaneous untwisting to the stable AB-stacking ($\theta = 0°$) occurs at 300 K (Fig. 2e), while a larger $L32 \times L32$ graphene flake exhibits negligible changes in θ even at temperatures of 1000 K (Fig. 2f).

We compute the total potential energy E_{θ}^{t}, relative to the global minimum energy E_{AB}^{t}, during untwisting of the various graphene flakes using a climbing-image nudged elastic band (NEB) method [21]. As shown in Fig. 3, we observe the existence of multiple energy barriers and local minimum potential energy states as the graphene flakes untwist from $\theta = \sim 8°$ to achieve the unrotated state constituting the global minimum at $\theta = 0°$ [12]. Increasing the flake size increases the number of potential energy barriers for untwisting as well as the magnitude of these energy barriers. The smallest $L1 \times L1$ graphene flake has exactly one local minimum at $\theta = \sim 8°$ with a low barrier energy of 0.052 eV (Fig. 3a), which explains the spontaneous untwisting at room temperature (Fig. 2e). For the $L2 \times L2$ graphene flake, two local minimums now develop at 7.13° and 3.47° with barrier energies of 0.17 eV and 0.31 eV, respectively (Fig. 3b). For the $L4 \times L4$ graphene flake, we observe four locally stable rotation angles (Fig. 3c) corresponding to the four transitional states in Figs. 2a-d. The initial state at $\theta = 7.34°$ is energetically unfavorable since it resides near a local peak, causing the graphene flake to rotate by a further $\Delta\theta = 0.58°$ to its local minimum energy state $\theta = 7.92°$ (Fig. 2a). The graphene flake has sufficient thermal energy to overcome the first energy barrier ($E_b = 0.36$ eV) at 600 K, and all but the final energy barrier ($E_b = 0.74$ eV) at 640 K. Slightly higher temperatures of 650 K allow crossing of the final energy barrier to reach the AB state. While the decreasing moving average of $E_\theta^t - E_{AB}^t$ with decreasing θ reflects the driving force for untwisting of the $L4 \times L4$ graphene flake, the increasing E_b imparts rotational stability. For the larger $L32 \times L32$ graphene flake, 32 energy barriers (each of $E_b = \sim$3-6 eV) corresponding to the 32 initial moiré superlattices along each direction are now observed (Fig. 3d). These multiple energy barriers provide rotational stability to the $L32 \times L32$ graphene flake even at high temperatures of 3000 K, comparable to the CVD temperatures for graphene growth. We remark that for a nanoribbon type geometry $Lm \times Ln$ with $m \neq n$, the number of locally stable states is governed by the number of initial moiré periods along the shorter dimension of the nanoribbon. An $L4 \times L32$ graphene nanoribbon, for example, is observed to undergo 4 distinct transitions initiating at temperatures of ~600 K before reaching the AB state.

Using an Arrhenius relation, the rate of transition from one rotational state (θ_1) to another (θ_2) can be expressed as $k_{\theta_1 \to \theta_2} = Ae^{-\frac{E_b}{k_B T}}$, where k_B is the Boltzmann constant. We obtain the potential energy barriers E_{b1} for five graphene flakes of increasing dimensions at the first stable state (θ_1) near the initial twist angle of $\theta = 7.34°$. We incrementally increase the temperature to determine the activation temperature T at which the graphene flake crosses E_{b1} and untwists to the neighboring stable state (θ_2). We approximate $k_{\theta_1 \to \theta_2}$ as the inverse of the activation time in our MD simulations for this first jump, and we summarize these parameters, along with the frequency pre-factor A, in Table 1. We note that increasing the flake size significantly increases E_{b1} and results in a higher activation temperature T for the first instance of untwisting. Because of the high E_{b1} of 3.93 eV for the largest $L32 \times L32$ graphene flake, we observe no untwisting of the graphene flake even at temperatures of 3000 K. For completeness, we include the subsequent barrier energies ($E_{b2}, E_{b3} \dots \dots$) for the graphene flakes and note a general trend of increasing number and magnitude of these energy barriers with increasing flake dimensions.

We have performed potential energy calculations for fully-periodic twisted graphene bilayers with complete moiré superlattices, scaled to the same number of atoms in a $L32 \times L32$ graphene flake for comparison purposes. We show a gradual but smooth decay of $E_{\theta}^{t} - E_{AB}^{t}$ (i.e. no energy barriers) with untwisting of fully-periodic moiré superlattices (dashed curve in Fig. 3d). In finite twisted graphene flakes, however, the moiré superlattices are truncated near the edges, which ultimately results in periodic fluctuations in the potential energy with untwisting. We quantify this incomplete periodicity of the moiré superlattices at the finite edges, r, as the remainder of the flake dimension L over the moiré period $L_p(\theta)$, and include its evolution with θ for the various graphene flakes in Fig. 3. Note that the twist angles at which r/L_p sharply transitions from 1 to 0 denote a fully-developed (untruncated) moiré pattern for the graphene flake, akin to fully-periodic twisted bilayer graphene. These discrete twist angles correspond to the saddle-point stacking configurations, with local energy minimum stacking configurations in between. During untwisting, each graphene flake crosses over a multitude of local minimum (and saddle-point) energy states equal to the initial number of moiré periods (4 for $L4 \times L4$; 32 for $L32 \times L32$).

The origin of the local minimum and saddle-point energy states can be traced to the incommensurability resulting in truncation of the moiré patterns at the edges, and can be conveniently described using a van der Waals dislocation model [22]. As shown in Fig. 4a and

4b, the per-atom potential energies for both twisted graphene E_θ as well as AB-stacked graphene E_{AB} are significantly higher at the edges due to asymmetric termination of carbon bonds. To remove this edge effect, we adopt $E_\theta - E_{AB}$ as a measure of the local change in energies associated with the twisted configuration relative to the global minimum AB stacking configuration (Fig. 4c). Atoms in the AB stacking configuration are already in the global minimum configuration and have $E_\theta - E_{AB}$ = 0, i.e. zero disregistry. Atoms in the BA stacking configuration are also in the global minimum configuration. However, these atoms have the maximum disregistry since they have opposite stacking to atoms in the AB configuration (stacking faults), as shown by the maximum differences in atomic energies ($E_\theta - E_{AB} = \pm 13$ meV). Therefore, the magnitude of the excess potential energy of each atom relative to that in its unrotated state, $|E_\theta - E_{AB}|$, constitutes a quantifiable measure of the extent of atom disregistry. We then classify groups of atoms based on the range of $|E_\theta - E_{AB}|$: AB (0-2.2 meV), AA (2.2-3.7 meV and 10-11.5 meV), SP (3.7-10 meV), and BA (11.5-13 meV), as shown in Fig. 4d. This energy-based descriptor enables easy identification and quantification of the AB and BA stacking domains separated by a network of partial dislocations (SP) and intersecting at the dislocation junctions (AA) with Burger's vectors $\frac{a_0}{3}[01\bar{1}0]$, $\frac{a_0}{3}[1\bar{1}00]$, and $\frac{a_0}{3}[\bar{1}010]$ as shown in the Supplementary Material [23], and is analogous to experimentally observed dark-field electron micrographs of as-grown bilayer graphene depicting alternating dark (AB) and bright (BA) domains [24,25].

Figure 5 shows contours of the atomic disregistry for the $L4 \times L4$ graphene flake at twist angles corresponding to the local minimum and saddle-point energy states along the minimum potential energy path in Fig. 3c. At the saddle point states, fully-periodic moiré patterns can now develop (Fig. 5a) because the flake dimension L is commensurate with the moiré period L_p. As a result, the barrier energy for interfacial sliding becomes very low since the stacking configurations of atoms in the periodic geometry is independent of the translational motion of the graphene flake relative to the substrate. In contrast, at twist angles corresponding to the local minimum energy states, L and L_p are strongly incommensurate and tend to minimize the total potential energy by favoring the presence of AB rather than AA stacking (Fig. 5b). Thus, small lattice shifts from this energy-minimized configuration can result in large changes in the stacking sequence for the incomplete moiré period at the edges, resulting in large barrier energies for both rotation and interfacial sliding. Consequently, the unstable SFEs or sliding energy barriers (without rotation) are higher at the local minimum energy states than at the neighboring saddle point states, as shown in the Supplementary Material [23]. We summarize the changes in the relative proportions of atoms with AA stacking (η_{AA}) as well as combined AB and BA stacking ($\eta_{\mathrm{AB+BA}}$) with untwisting of all four graphene flakes in Fig. 6. We note that the local peaks of η_{AA} coincide with the valleys of $\eta_{\mathrm{AB+BA}}$ and correspond to the unstable saddle-point energy states (U). Similarly, the valleys of η_{AA} coincide with the peaks of $\eta_{\mathrm{AB+BA}}$ and correspond to the locally stable minimum energy states (S).

4. Barrier Energy Model

Our above results show that the number of locally-stable energy states and their barrier energies for untwisting of bilayer graphene scale with the flake size. Consider a graphene flake of dimensions $nL_p^{\theta_0} \times nL_p^{\theta_0}$ and with initial twist angle θ_0, where $L_p^{\theta_0}$ denotes the moiré periodicity and n is the number of moiré periods along each flake dimension at θ_0. During untwisting to the stable AB-state, a total of n locally-stable energy states will be observed along the minimum potential energy path separated by $\frac{\theta_0}{n}$ equal intervals. At these energy minimum states, the area encompassed by the truncated moiré patterns at the edges of the twisted flake is considered as the edge area, and is given by

$$A_{edge} = r_c\left(2nL_p^{\theta_0} - r_c\right)\sin\frac{\pi}{3} \tag{1}$$

where r_c is the remainder of the flake dimension $nL_p^{\theta_0}$ over the current moiré period L_p at the minimum energy states (i.e. $r = r_c$) and is consistently shown to be

$$r_c = \sim L_p/3 \tag{2}$$

across all flake dimensions in Fig. 3 except at small θ. The discrete twist angles corresponding to each minimum energy state can be expressed as

$$\theta_c = \theta_0 + \frac{\theta_0}{n}\left(\frac{r_c}{L_p} - b + 1\right) \tag{3}$$

where $b(= 1 \dots\dots n)$ is the number of barrier crossings during untwisting starting from the first barrier crossing $b = 1$ at θ_0. Note that θ_0 is one of the saddle points, and the graphene flake first settles to its minimum energy state at $b = 1$ with corresponding twist angle $\theta_0 + \frac{\theta_0}{3n}$. Since $L_p = a_0/\left(2\sin\frac{\theta}{2}\right)$ where $a_0 = 2.46$ Å is the graphene lattice constant [26], we obtain a semi-analytical expression from (1) to (3) relating A_{edge} with the flake dimension $nL_p^{\theta_0}$ at the n locally-stable energy states along the minimum potential energy path.

Figure 7a shows the cross-plot of the first potential energy barrier E_{b1} versus the edge area A_{edge} for seven graphene flakes of increasing dimensions ($nL_p^{\theta_0}$) at the first stable state near the initial twist angle of $\theta_0 = 7.34°$ ($b = 1$). Since A_{edge} scales almost linearly with the flake edge dimension ($nL_p^{\theta_0}$) per (1), the similar linear relationship between E_{b1} and A_{edge} confirms that the proportional increase in the area encompassing the incomplete moiré period at the finite flake edges is responsible for the increased barrier energies for untwisting with flake size. This increased edge area allows greater propensity for larger flakes to minimize the total potential energy by favoring the presence of AB rather than AA stacking. This sole dependence of the barrier energy on the edge area encompassing the truncated moiré periods suggests that the results here are general and not dependent on the flake shape. Approximating a barrier energy density of $dE_b/dA_{edge} = 0.64\ \mathrm{meV/Å^2}$ from Fig. 7a, we can then predict all the $b = 1 \ldots \ldots n$ barrier energies for various flake sizes, as shown in Fig. 7b. Our analytical predictions (solid lines) are in excellent agreement with our simulation results (symbols) for the first couple of barrier energies. At larger b, however, some deviations from the analytical predictions are observed, potentially due to validity of the constant barrier energy density assumption (based on $b = 1$) as well as a shift in r_c at small θ close to the AB state (Fig. 3).

5. Discussion and Conclusion

The multiple energy barriers governing rotational stability of twisted graphene flakes result in the thermally-driven rotation of bilayer graphene from its incommensurate twisted stacking at $\theta = 7.34°$ into commensurate AB stacking as observed experimentally [10], and also explain the depletion of twisted bilayer graphene with $\theta < 4°$ during CVD growth [5]. Our studies here show that the edge effect drives the rotation of twisted homogeneous nanometer-sized atomic sheet layers governed by pure van der Waals interactions. For inhomogeneous systems consisting of twisted 2D atomic sheets of different crystal lattices, it has been reported that bulk effects arising from elastic lattice mismatch energies can drive self-rotations at much larger (macroscopic) scales [27].

One consequence of incommensurability is the smaller interfacial binding leading to superlubricity along the twisted graphene interface. For example, graphitic mesas on bulk graphite surfaces subjected to mechanical loading via surface probe tips are reported to undergo smooth sliding followed by sudden rotation into stable locked-in positions [9]. Similarly, sliding of graphene flakes (averaging 12.5 nm in size, comparable to $L6 \times L6$) on graphene reveal a tip-induced rotation of the flakes from a commensurate to an incommenstrate registry prior to rapid sliding [10]. As shown by our SFE calculations in the Supplementary Material [23], the dramatic decrease in the sliding barrier energies with increasing θ suggests that it may be energetically favorable for an AB-stacked graphene flake to rotate into its twisted form before sliding, which explains the experimental observations. Interestingly, the superlubric experiments demonstrate longer sliding distances at lower than at higher temperatures, potentially because of the higher probability of overcoming the potential energy barriers to rotate back to the stable AB state at higher temperatures as shown in Table 1. These superlubric experiments also suggest a bias towards smaller-sized graphene samples in displaying such transitional twisting and untwisting behaviors [14]. Separately, atomic force microscopy studies on the driven dynamics of a finite graphite flake on a graphite surface show that larger flakes and low temperature conditions induce superlubric sliding without rotation, while smaller flakes or higher temperatures lead to flake rotation [28]. These experimental observations are in good agreement with the size- and temperature-dependence exhibited by our twisted graphene bilayers.

The observed rotational transitions for twisted bilayer graphene (E_b per area $\sim$7 to 15 meV/nm^2 for $L4 \times L4$ flakes) are applicable to interfacial systems governed by weak van der

Waals interactions, such as graphene physisorbed on aluminum or titanium oxide (E_b per area ~3 to 40 meV/nm^2) [29] or graphene on h-BN (E_b per area ~319 meV/nm^2) [20]. In fact, the existence of multiple barriers for stepwise untwisting is solely a crystallographic phenomenon, and we expect similar energy landscapes and evolution in moiré patterns during untwisting of all bicrystal structures. Nevertheless, thermally-driven rotation may not spontaneously occur because of the high barrier energies associated with covalently or metallically-bonded bicrystals, such as graphene chemisorbed on titanium (E_b~2.2 eV/nm^2) [29], and metallic bicrystals with twist grain boundaries (E_b~1.5 eV/nm^2) [30].

In summary, finite edge effects arising from truncation of the moiré pattern control the rotational stability of finite, twisted 2D materials of the same type. Specifically, the varying moiré periodicity during untwisting of the bilayer material generates multiple potential energy barriers due to the spatially varying degree of commensurability in atom stackings. These edge effects explain the underpinning mechanisms for rotational transitions of such structures, as well as the size- and temperature-dependence for such transitions. Results have significant implications for the design of twisted 2D structures for nanotribological and nanoelectronic applications.

Acknowledgements

The authors (SB & HBC) acknowledge the support provided by Dr. Ali Sayir under the AFOSR Aerospace Materials for Extreme Environment Program (award no. FA9550-19-1-0242). HJ acknowledges the support of the Army Research Office (W911NF-17-1-0544) Material Science Division under Dr. Chakrapani Varanasi, and support from NSF grant number CMMI 18-25300 (MOMS program). Many fruitful discussions with collaborators and group members of HJ, including Dr. Pascal Pochet, Prof. Elif Ertekin, Dr. Shuze Zhu, and Emil Annevelink, are gratefully acknowledged. We acknowledge computational time provided by the Blue Waters sustained-petascale computing project, which is supported by the National Science Foundation (awards OCI-0725070 and ACI-1238993) and the state of Illinois. Blue Waters is a joint effort of the University of Illinois at Urbana-Champaign and its National Center for Supercomputing Applications.

References:

[1] A. K. Geim and I. V. Grigorieva, Nature (London) **499**, 419 (2013).
[2] K. S. Novoselov, A. Mishchenko, A. Carvalho, and A. H. Castro Neto, Science **353**, 461 (2016).
[3] R. Ribeiro-Palau, C. Zhang, K. Watanabe, T. Taniguchi, J. Hone, and C. R. Dean, Science **361**, 690 (2018).
[4] A. Harpale, M. Panesi, and H. B. Chew, J. Chem. Phys. **142**, 061101 (2015).
[5] L. Brown, R. Hovden, P. Huang, M. Wojcik, D. A. Muller, and J. Park, Nano Lett. **12**, 1609 (2012).
[6] H. Yoo, R. Engelke, S. Carr, S. Fang, K. Zhang, P. Cazeaux, S. H. Sung, R. Hovden, A. W. Tsen, T. Taniguchi, K. Watanabe, G. C. Yi, M. Kim, M. Luskin, E. B. Tadmor, E. Kaxiras, and P. Kim, Nat. Mater. **18**, 448 (2019).
[7] Y. Cao, V. Fatemi, A. Demir, S. Fang, S. L. Tomarken, J. Y. Luo, J. D. Sanchez-Yamagishi, K. Watanabe, T. Taniguchi, E. Kaxiras, R. C. Ashoori, and P. Jarillo-Herrero, Nature (London) **556**, 80 (2018).
[8] M. Dienwiebel, G. S. Verhoeven, N. Pradeep, J. W. M. Frenken, J. A. Heimberg, and H. W. Zandbergen, Phys. Rev. Lett. **92**, 126101 (2004).
[9] C. Qu, S. Shi, M. Ma, and Q. Zheng, Phys. Rev. Lett. **122**, 246101 (2019).
[10] X. Feng, S. Kwon, J. Y. Park, and M. Salmeron, ACS Nano **7**, 1718 (2013).
[11] Y. Cao, V. Fatemi, S. Fang, K. Watanabe, T. Taniguchi, E. Kaxiras, and P. Jarillo-Herrero, Nature (London) **556**, 43 (2018) (2018).
[12] K. Seo, V. N. Kotov, and B. Uchoa, Phys. Rev. Lett. **122**, 246402 (2019).
[13] S. Zhu, P. Pochet, and H. T. Johnson, ACS Nano **13**, 6925 (2019).
[14] Q. Zheng, B. Jiang, S. Liu, Y. Weng, L. Lu, Q. Xue, J. Zhu, Q. Jiang, S. Wang, and L. Peng, Phys. Rev. Lett. **100**, 1 (2008).
[15] Z. Liu, J. Yang, F. Grey, J. Z. Liu, Y. Liu, Y. Wang, Y. Yang, Y. Cheng, and Q. Zheng, Phys. Rev. Lett. **108**, 205503 (2012).
[16] A. E. Filippov, M. Dienwiebel, J. W. M. Frenken, J. Klafter, and M. Urbakh, Phys. Rev. Lett. **100**, 1 (2008).
[17] S. Plimpton, J. Comput. Phys. **117**, 1 (1995).
[18] D. W. Brenner, O. A. Shenderova, J. A. Harrison, S. J. Stuart, B. Ni, and S. B. Sinnott, J. Phys. Condens. Matter **14**, 783 (2002) .
[19] A. N. Kolmogorov and V. H. Crespi, Phys. Rev. B **71**, 235415 (2005).
[20] S. Zhou, J. Han, S. Dai, J. Sun, and D. J. Srolovitz, Phys. Rev. B **92**, 155438 (2015).
[21] G. Henkelman, B. P. Uberuaga, and H. Jónsson, J. Chem. Phys. **113**, 9901 (2000).
[22] P. Pochet, B. C. McGuigan, J. Coraux, and H. T. Johnson, Appl. Mater. Today **9**, 240 (2017).
[23] See Supplemental Material at [URL will be inserted by publisher] for dislocation network, disregistry, and density, as well as stacking fault energy surfaces corresponding to saddle point and local minimum energy states in twisted bilayer graphene.
[24] J. S. Alden, A. W. Tsen, P. Y. Huang, R. Hovden, L. Brown, J. Park, D. A. Muller, and P. L. McEuen, Proc. Natl. Acad. Sci. U. S. A. **110**, 11256 (2013).
[25] B. Butz, C. Dolle, F. Niekiel, K. Weber, D. Waldmann, H. B. Weber, B. Meyer, and E.

Spiecker, Nature (London) **505**, 533 (2014).

[26] M. M. Van Wijk, A. Schuring, M. I. Katsnelson, and A. Fasolino, Phys. Rev. Lett. **113**, 1 (2014).

[27] K. M. Omambac, H. Hattab, C. Brand, G. Jnawali, A. T. N'Diaye, J. Coraux, R. van Gastel, B. Poelsema, T. Michely, F.-J. Meyer zu Heringdorf, and M. H. Hoegen, Nano Lett. **19**, 4594 (2019).

[28] A. S. De Wijn, C. Fusco, and A. Fasolino, Phys. Rev. E **81**, 046105 (2010).

[29] S. Bagchi, C. Ke, and H. B. Chew, Phys. Rev. B **98**, 174106 (2018).

[30] R. Li and H. B. Chew, Philos. Mag. **95**, 1029 (2015).

Table 1: Activation energetics for untwisting of bilayer graphene

Flake Size	$E_{b1,}\, E_{b2}\,, E_{b3}\; \ldots \ldots E_{bfinal}$ (eV)	A (ps^{-1}) for E_{b1}	T (K) for E_{b1}
$L1 \times L1$	0.052	0.22	150
$L2 \times L2$	0.17, 0.31	5.66	300
$L4 \times L4$	0.36, 0.55, 0.79, 0.74	22.56	600
$L6 \times L6$	0.62, 0.79, 1.14, 1.42, 1.02, 0.66	228.83	700
$L32 \times L32$	3.93, 4.45, 4.71, 4.45, ……6.6	-	>3000

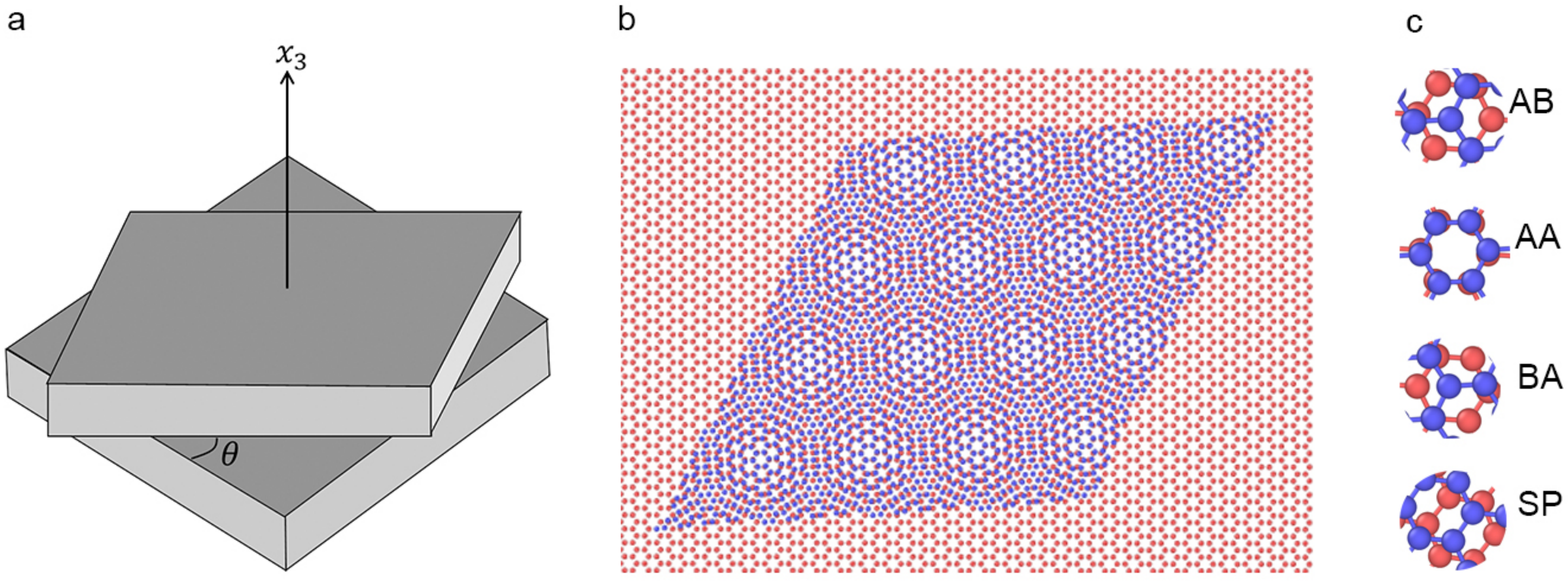
a
x_3
θ
b
c
AB
AA
BA
SP

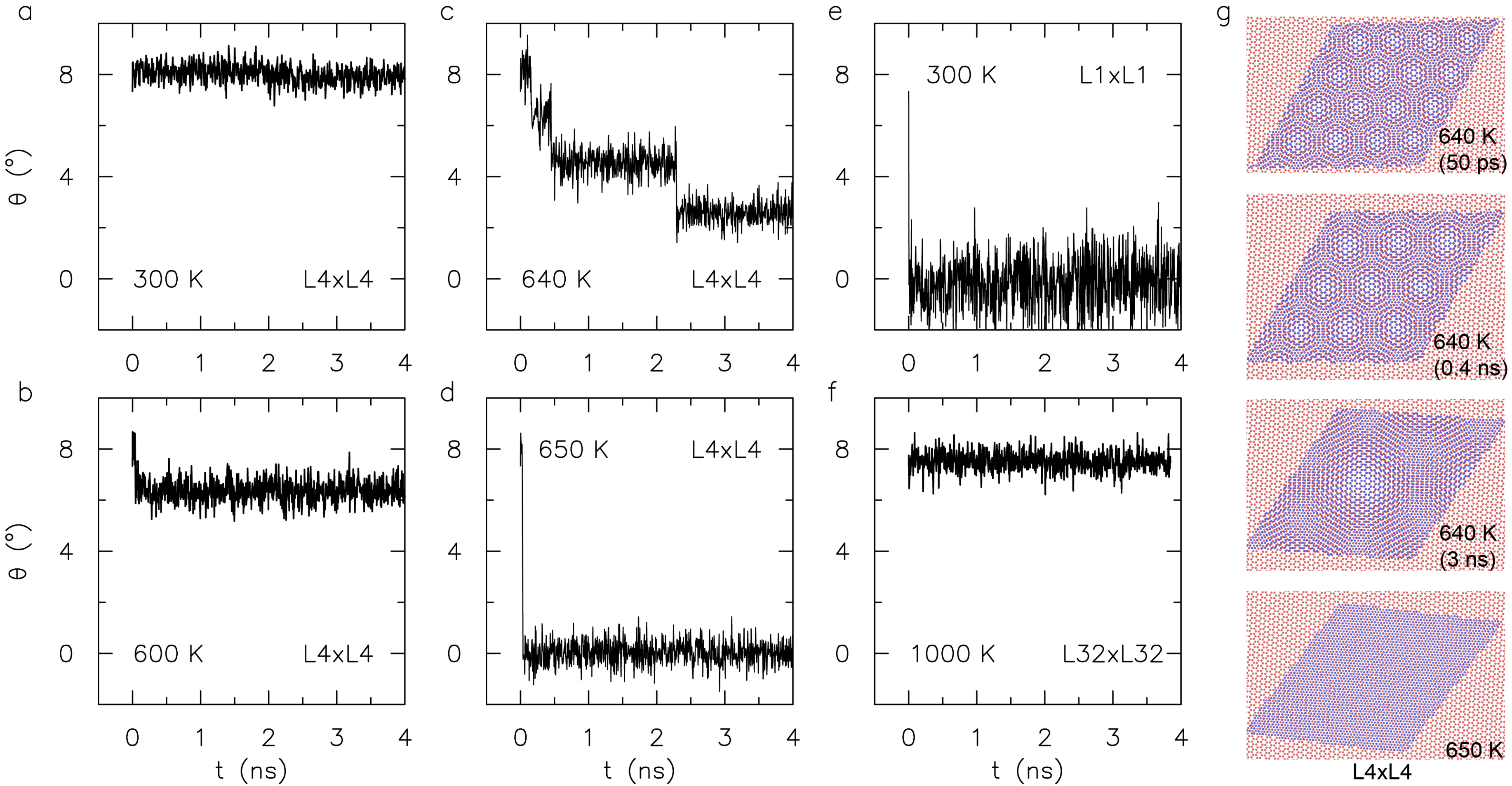
a
b
c
d
e
f
g
θ (°)
t (ns)
0
4
8
0
1
2
3
4
300 K
L4xL4
600 K
L4xL4
640 K
L4xL4
650 K
L4xL4
300 K
L1xL1
1000 K
L32xL32
640 K
(50 ps)
640 K
(0.4 ns)
640 K
(3 ns)
650 K
L4xL4

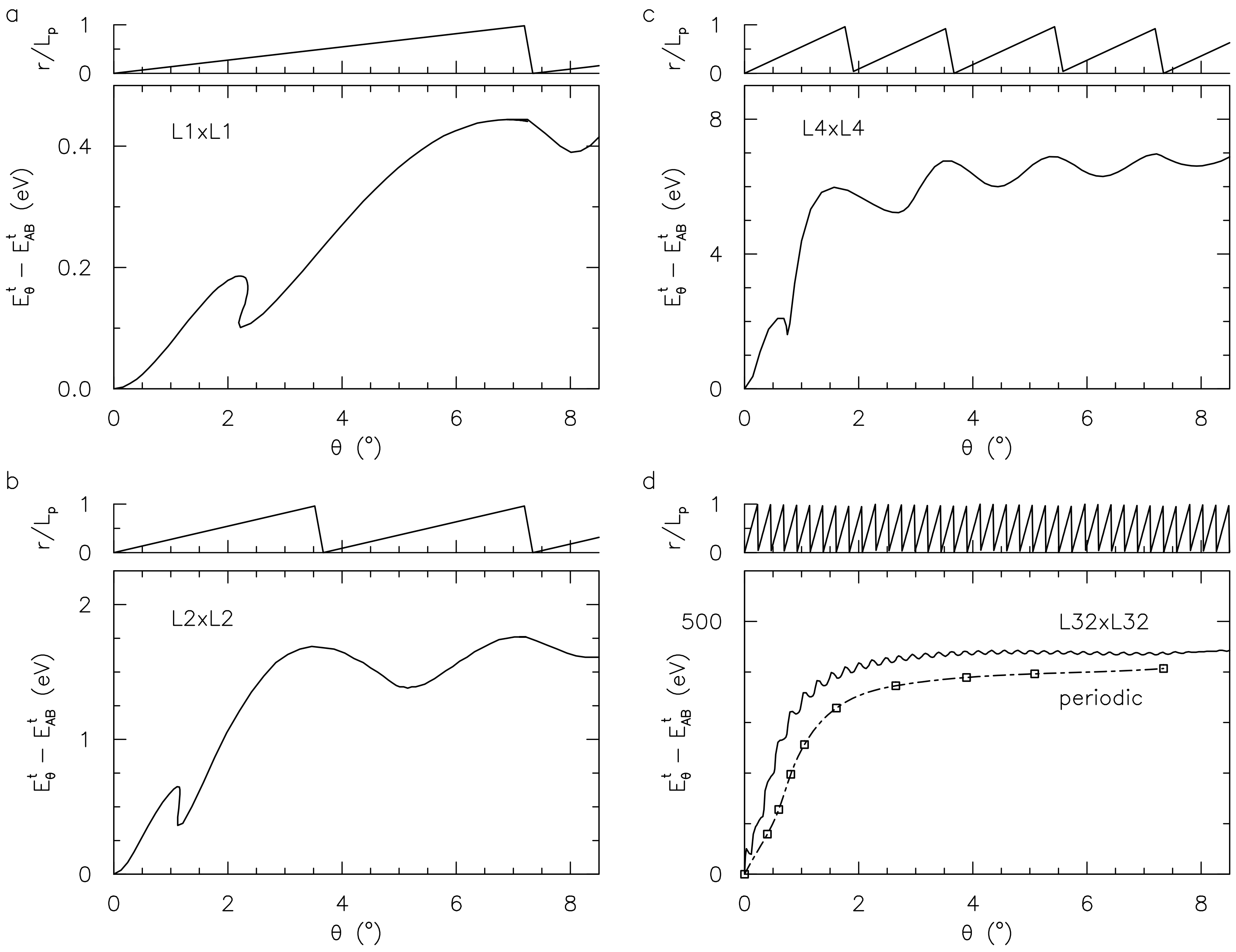
a
b
c
d
r/L$_p$
0
1
$E^t_\theta - E^t_{AB}$ (eV)
0.0
0.2
0.4
0
1
2
4
8
500
θ (°)
0
2
4
6
8
L1xL1
L2xL2
L4xL4
L32xL32
periodic

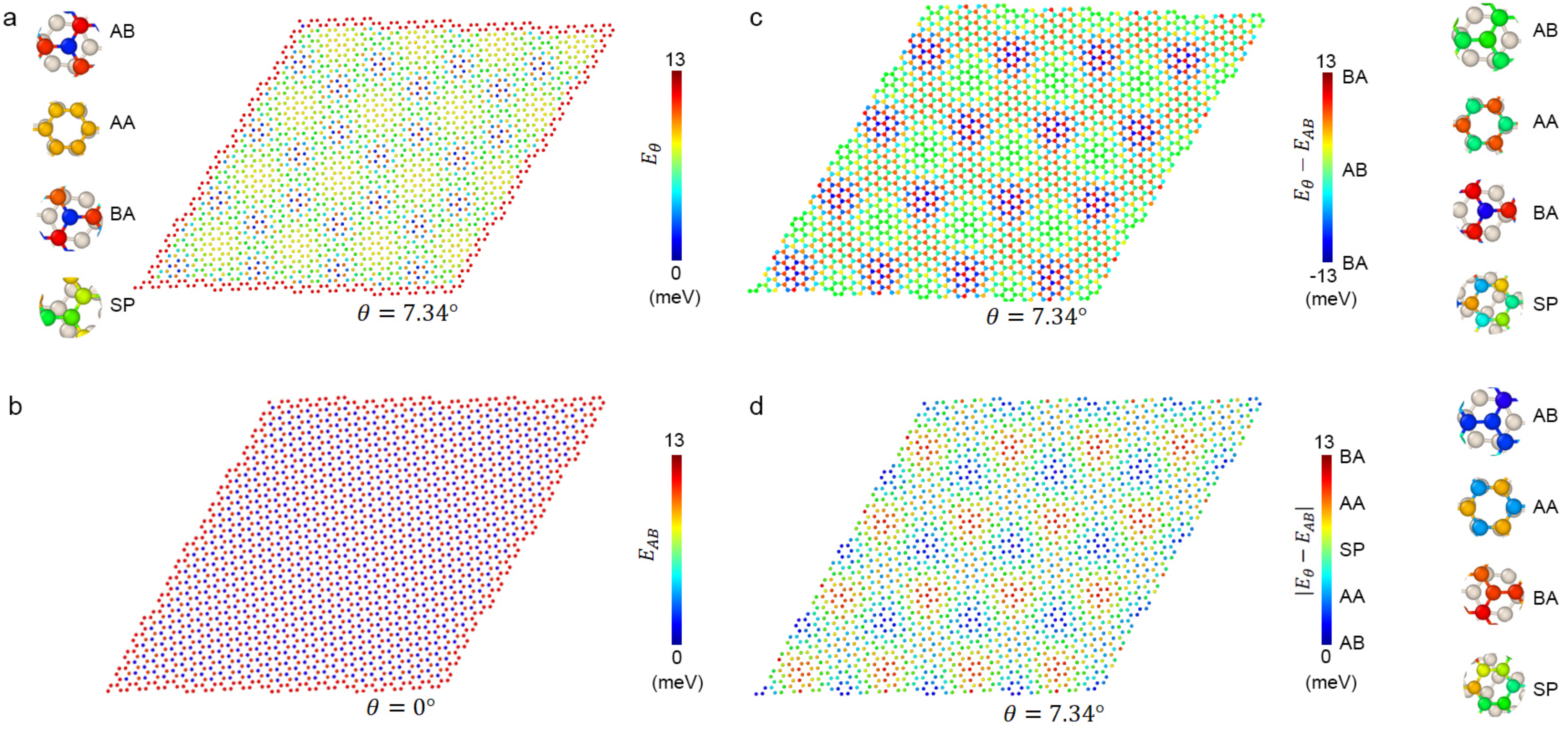
a
AB
AA
BA
SP
$\theta = 7.34°$
13
E_θ
0
(meV)
b
$\theta = 0°$
13
E_{AB}
0
(meV)
c
$\theta = 7.34°$
13
BA
$E_\theta - E_{AB}$
AB
-13
BA
(meV)
AB
AA
BA
SP
d
$\theta = 7.34°$
13
BA
AA
SP
AA
AB
0
$|E_\theta - E_{AB}|$
(meV)
AB
AA
BA
SP

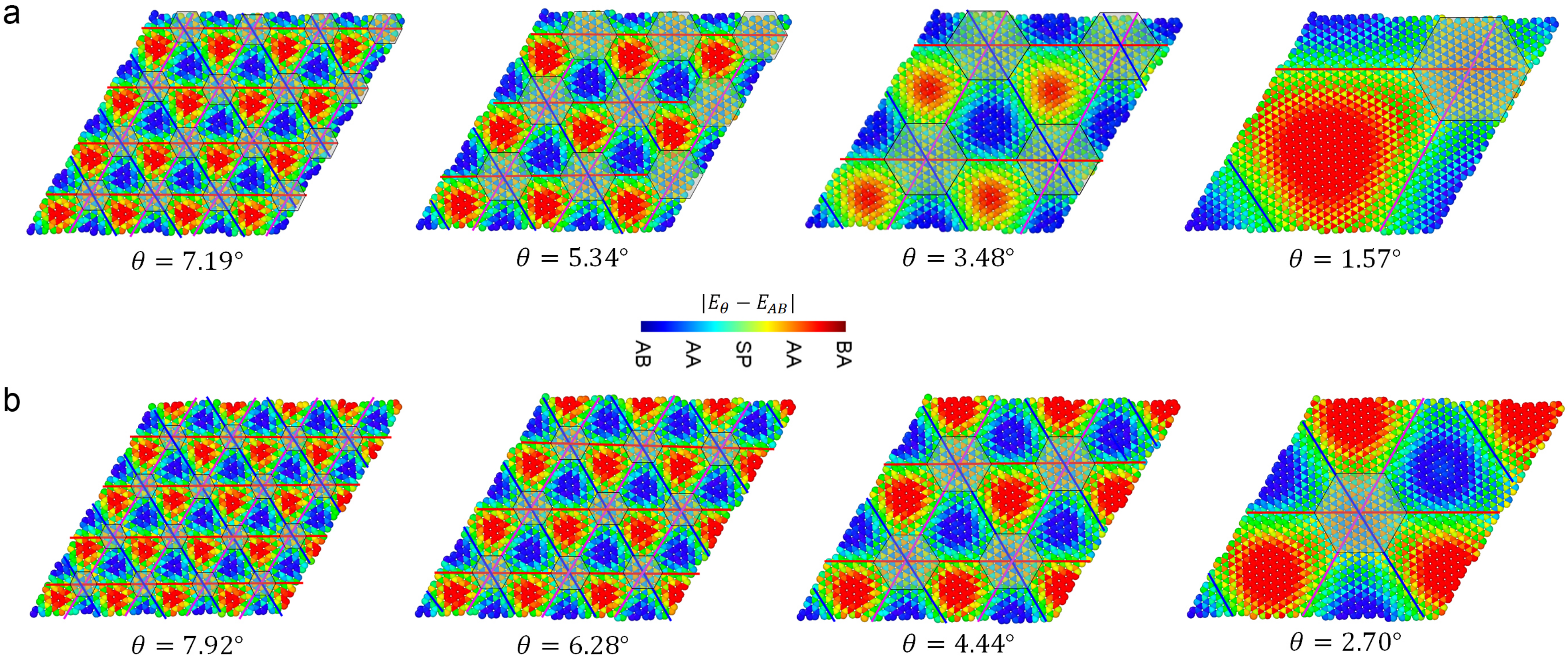
a
θ = 7.19°
θ = 5.34°
θ = 3.48°
θ = 1.57°
$|E_\theta - E_{AB}|$
AB
AA
SP
AA
BA
b
θ = 7.92°
θ = 6.28°
θ = 4.44°
θ = 2.70°

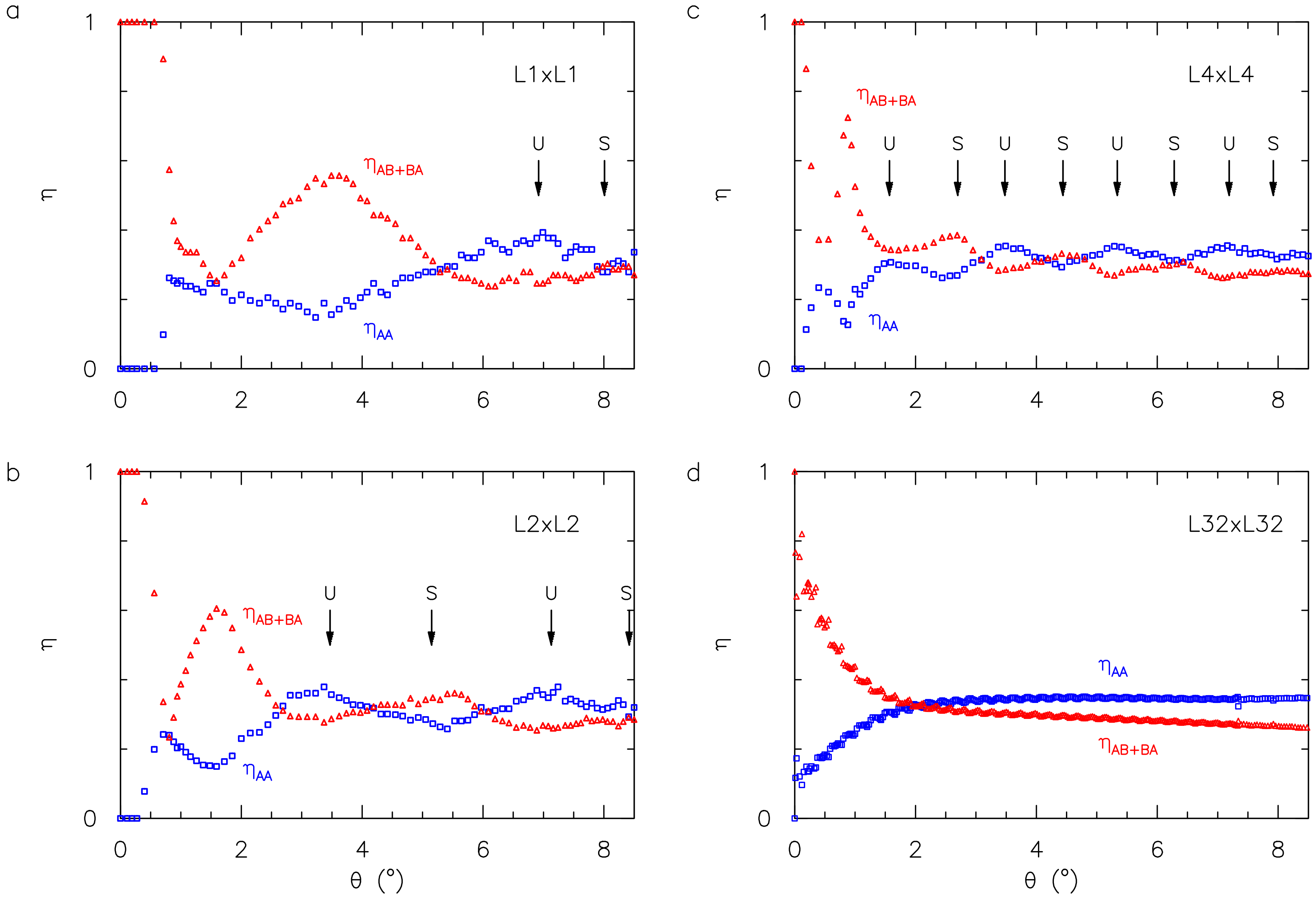
a
L1xL1
U
S
ηAB+BA
ηAA
η
1
0
0
2
4
6
8
b
L2xL2
U
S
U
S
ηAB+BA
ηAA
η
1
0
0
2
4
6
8
θ (°)
c
L4xL4
U
S
U
S
U
S
U
S
ηAB+BA
ηAA
η
1
0
0
2
4
6
8
d
L32xL32
ηAA
ηAB+BA
η
1
0
0
2
4
6
8
θ (°)

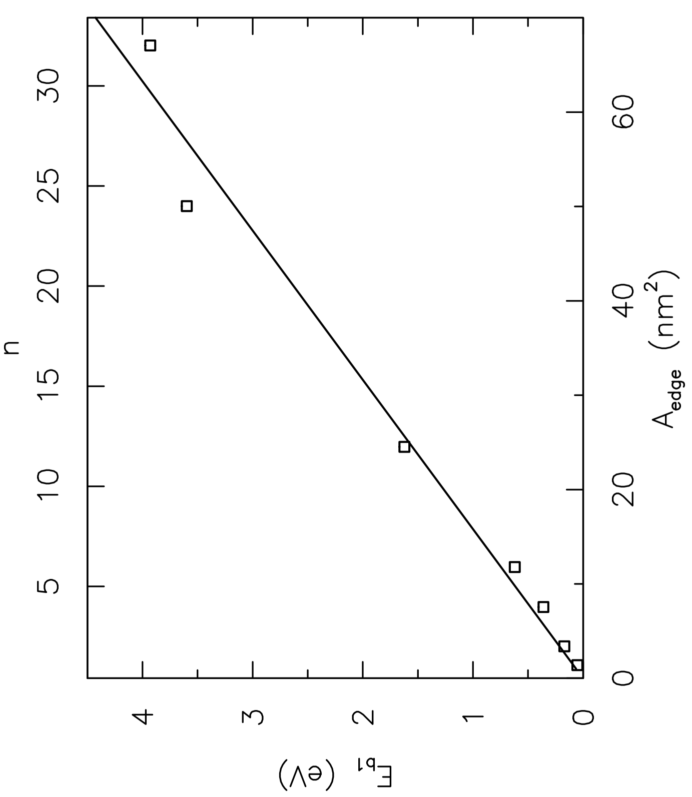
n
5
10
15
20
25
30
E_{b1} (eV)
0
1
2
3
4
0
20
40
60
A_{edge} (nm^2)

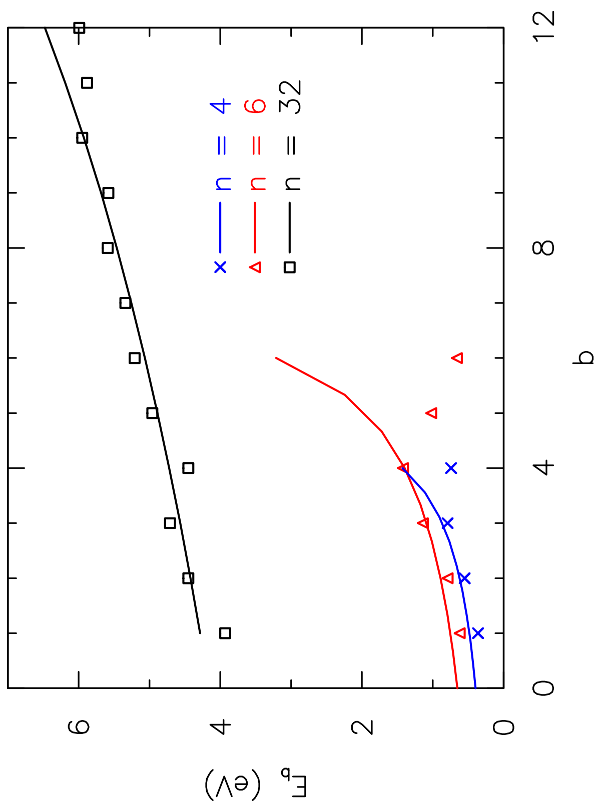
E_b (eV)
0
2
4
6
0
4
8
12
b
n = 4
n = 6
n = 32